



Full length article

Thermal stability and mechanical properties of sputtered (Hf,Ta,V,W,Zr)-diborides

A. Kirnbauer^{a,*}, A. Wagner^a, V. Moraes^a, D. Primetzhofer^b, M. Hans^c, J.M. Schneider^c, P. Polcik^d, P.H. Mayrhofer^a

^aInstitute of Materials Science and Technology, TU Wien, 1060 Vienna, Austria

^bDepartment of Physics and Astronomy, Uppsala University, 75120 Uppsala, Sweden

^cMaterials Chemistry, RWTH Aachen University, 52074 Aachen, Germany

^dPlansee Composite Materials GmbH, 86983 Lechbruck am See, Germany

ARTICLE INFO

Article history:

Received 23 July 2020

Revised 29 August 2020

Accepted 5 September 2020

Available online 10 September 2020

Keywords:

High-entropy alloys (HEAs)

Magnetron sputtering

multi-element diborides

Thermal stability

High-entropy sublattice (HES)

ABSTRACT

Non-reactive magnetron sputtering of a diboride target composed of HfB₂, TaB₂, VB₂, W₂B₅, and ZrB₂ with equimolar composition leads to the formation of crystalline single-phase solid solution diboride thin films, (Hf,Ta,V,W,Zr)B₂, with a high-entropy metal-sublattice. Their growth morphology (dense and fine-fibrous), crystal structure (AlB₂-type), as well as mechanical properties (indentation modulus E of ~580 GPa and hardness H of ~45 GPa), and chemical compositions are basically independent of the substrate bias potential applied (varied between -40 and -100 V) during the deposition at 450°C.

Detailed X-ray diffraction (XRD) and atom probe tomography (APT) studies indicate that the (Hf,Ta,V,W,Zr)B₂ thin films remain single-phase AlB₂-structured (with randomly distributed elements at the metal-sublattice) during vacuum-annealing at temperatures up to 1200°C. Only when increasing the annealing temperature to 1400°C, the formation of small orthorhombic structured (V,W)B-based regions can be detected, indicating the onset of decomposition of (Hf,Ta,V,W,Zr)B₂ thin films into (Hf,Ta,Zr)B₂ and (V,W)B, accompanied by the formation of confined B-rich boundary regions between these phases. After annealing at 1400°C the hardness is still very high with ~44 GPa, as the volume fraction of the newly formed (V,W)B-rich domains is small and the majority of the coating is still solid-solution (Hf,Ta,V,W,Zr)B₂ with severe lattice distortions. Only at even higher T_a of 1500 and 1600 °C, H decreased to ~39 GPa.

© 2020 Acta Materialia Inc. Published by Elsevier Ltd.

This is an open access article under the CC BY-NC-ND license (<http://creativecommons.org/licenses/by-nc-nd/4.0/>)

1. Introduction

The demand for materials able to withstand high temperatures and mechanical loads is connected with new technological developments. Therefore, these are in focus of many research activities. The development of protective thin film materials has the advantage of combining basic materials science concepts with the huge and versatile variety in process conditions accessible through physical vapour deposition (like magnetron sputtering). A relatively new alloying concept – equiatomic multicomponent alloys with at least five principal elements – was introduced by Cantor in 2004 [1]. As these alloys exhibit a configurational entropy ΔS_{conf} of >

$1.5 \cdot R$, with R being the universal gas constant, the term high-entropy alloys (HEA) was introduced by Yeh et al. [2] also in 2004.

In addition to HEAs a corresponding high-entropy concept has also been applied to ceramic materials including borides, carbides, and oxides. According to Murty, Yeh, and Ranganathan, ceramics are considered as high-entropy materials if they consist of five binary ceramic phases [3]. Here we want to mention that it is probably not the high configurational entropy per se leading to substantially enhanced material properties like strength, toughness, thermal stability, and oxidation resistance. Only if the single-phase alloys (or the matrix of a more complex material) are composed of at least 5 principal elements (leading to $\Delta S_{\text{conf}} > 1.5 \cdot R$) they outperform conventional alloys (which are typically based only on 1, 2, or 3 principal elements). Connected with this condition (at least 5 principal elements) is not only a high configurational entropy but also a severe lattice distortion, a sluggish diffusion, and a cocktail

* Corresponding author.

E-mail address: alexander.kirnbauer@tuwien.ac.at (A. Kirnbauer).

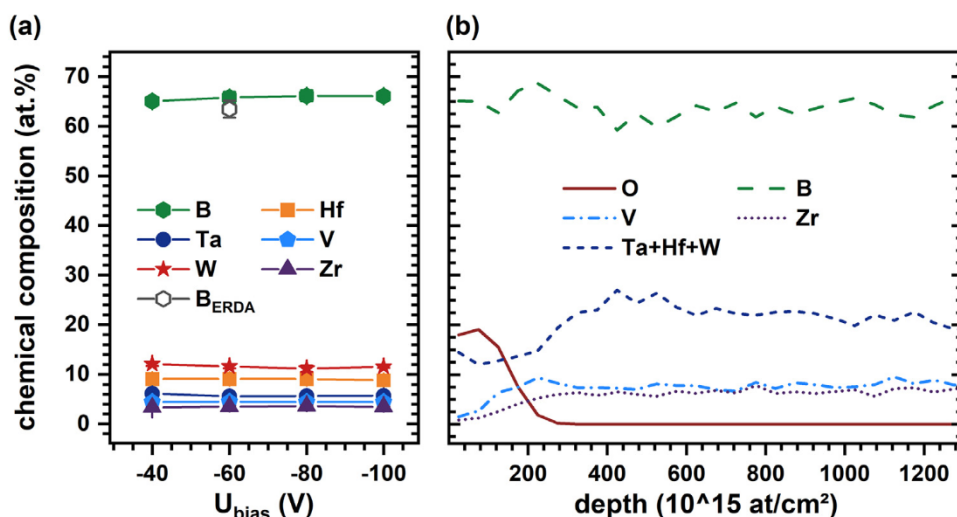


Fig. 1. (a) EDS obtained chemical composition of $(\text{Hf,Ta,V,W,Zr})\text{B}_2$ coatings on sapphire substrates, prepared with $U_{\text{bias}} = -40, -60, -80$, and -100 V. For comparison also the ERDA obtained B content is added for the sample prepared with $U_{\text{bias}} = -60$ V. (b) ERDA depth profile for the sample prepared with $U_{\text{bias}} = -60$ V.

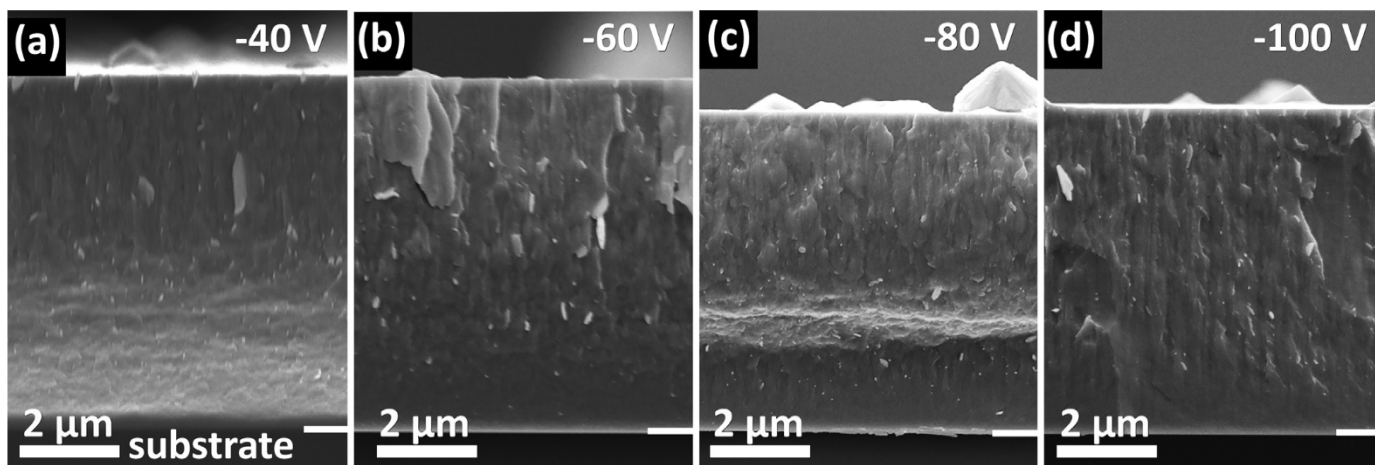


Fig. 2. SEM fracture cross-sections of $(\text{Hf,Ta,V,W,Zr})\text{B}_2$ coatings deposited with $U_{\text{bias}} =$ (a) -40 V, (b) -60 V, (c) -80 V, and (d) -100 V on sapphire substrates.

effect (cumulative properties and positive deviation from the arithmetic mean value, i.e., like a cocktail being more colourful and arched or more colourful and tastier than its components). More recently, we proposed to refer to such compounds as high-entropy metal-sublattice ceramics [4]. Based on the HEA concept, borides, carbides, and oxides in bulk form have been studied regarding their mechanical properties, thermal stability, and oxidation resistance. Also these often show significantly improved materials characteristics compared to their constituting binaries [5–11]. Later, such a high-entropy concept for ceramic materials was also applied to thin films. First investigations concentrated on $(\text{Al,Cr,Ta,Ti,Zr})\text{N}$ coatings, which exhibit minor dependence of their structural and mechanical properties on varying the deposition parameters such as reactive gas flow, substrate bias potential, and substrate temperature [12–14]. Additionally, this material system shows excellent thermal stability and diffusion barrier abilities for Cu [15]. Further studies on such thin films (actually composed of sublattice(s) with a high entropy) include investigations of refractory metal nitrides as well as oxide coatings with attractive mechanical properties and improved thermal stability [4],[16]. Recent investigations on diborides highlighted the potential in improving ceramic-like thin film materials when containing a high-entropy metal-sublattice [17]. In analogy to the HEA concept, and based on our

previous studies [4],[17], we suggest that the term “high-entropy sublattice (HES) concept” would be more adequate for multicomponent ceramic thin film materials, if the configuration entropy of at least one sublattice exceeds $1.5 \cdot R$.

Here, we study the phase formation, thermal stability and mechanical properties of single-phase solid solution $(\text{Hf,Ta,V,W,Zr})\text{B}_2$ developed by non-reactive magnetron sputtering of a powder-metallurgically produced compound target. The material system was chosen based on previous studies on binary and ternary diboride coatings within the system Hf-Ta-V-W-Zr [17–20] and after discussion with the target manufacturer. To avoid any confusion, we mention that we use the term binary diboride (carbide, nitride, or oxide) for compounds containing one other element aside from B (C, N, or O). Hence, to connect the term with the underlying binary system as well as binary phases, as done previously [44,45]. The corresponding terminology applies to ternary and higher order diborides (carbides, nitrides, or oxides). The developed high-entropy metal-sublattice diboride (HESB) thin films show no significant dependence on the bias potential used during deposition, based on investigations by X-ray diffraction (XRD), scanning electron microscopy (SEM), and nanoindentation. Therefore, only the coating prepared with a bias potential of -60 V was further investigated with respect to thermal stability, for which we used

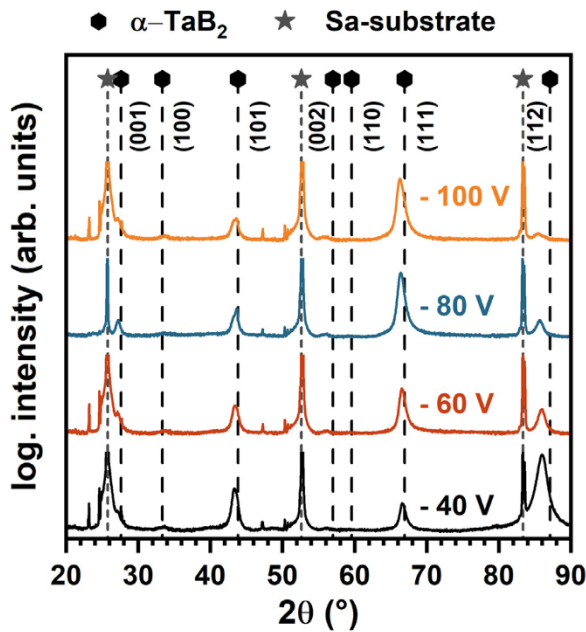


Fig. 3. XRD patterns of $(\text{Hf,Ta,V,W,Zr})\text{B}_2$ coatings deposited on sapphire substrates with $U_{\text{bias}} = -40, -60, -80, \text{ and } -100 \text{ V}$. The α -structure is indicated by an α - TaB_2 (ICDD 00-038-1462) as this reference pattern yields the closest match to the solid solution $(\text{Hf,Ta,V,W,Zr})\text{B}_2$, substrate peak positions are indicated by grey stars.

detailed XRD, nanoindentation (hardness H and indentation modulus E), elastic recoil detection analysis (ERDA), and atom probe tomography (APT).

2. Experimental and methods

The $(\text{Hf,Ta,V,W,Zr})\text{B}_2$ thin films were deposited by unbalanced non-reactive magnetron sputtering with a modified Leybold Z400 deposition system using four different bias potentials ($U_{\text{bias}} = -40,$

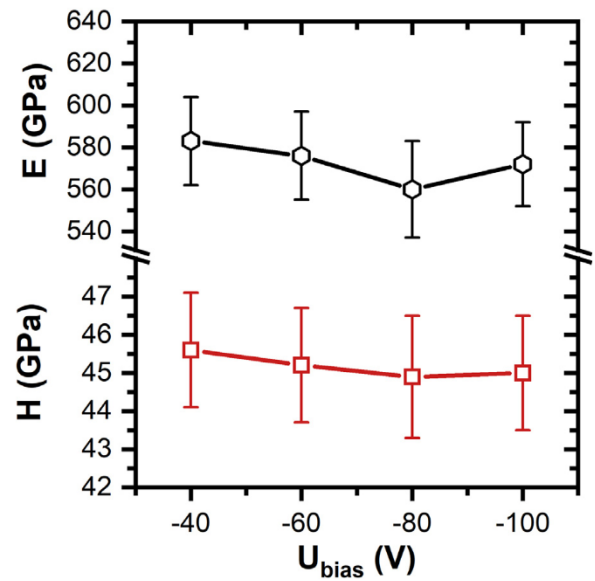


Fig. 4. Indentation modulus E and hardness H of single-phased solid solution $(\text{Hf,Ta,V,W,Zr})\text{B}_2$ coatings on sapphire substrates deposited with $U_{\text{bias}} = -40, -60, -80, \text{ and } -100 \text{ V}$.

$-60, -80, -100 \text{ V}$). We used one powder-metallurgically produced 3-inch composite diboride target consisting of 20 mol% HfB_2 , TaB_2 , VB_2 , W_2B_5 , and ZrB_2 . The target-to-substrate distance (in a parallel concentric arrangement) was 4 cm. The substrates (polycrystalline Al_2O_3 and sapphire (1-102) platelets, and low alloyed steel foil) were ultrasonically cleaned in acetone and ethanol for 10 min prior to loading to the deposition chamber. After reaching a base pressure of $\leq 0.3 \text{ mPa}$ they were Ar-ion etched with -150 V pulsed DC (150 kHz, 2496 ns) at an Ar gas pressure of 1.3 Pa. During deposition, the substrate temperature (T_s) was 450°C , the Ar gas pressure was 0.35 Pa (Ar gas flow rate of 30 sccm), the

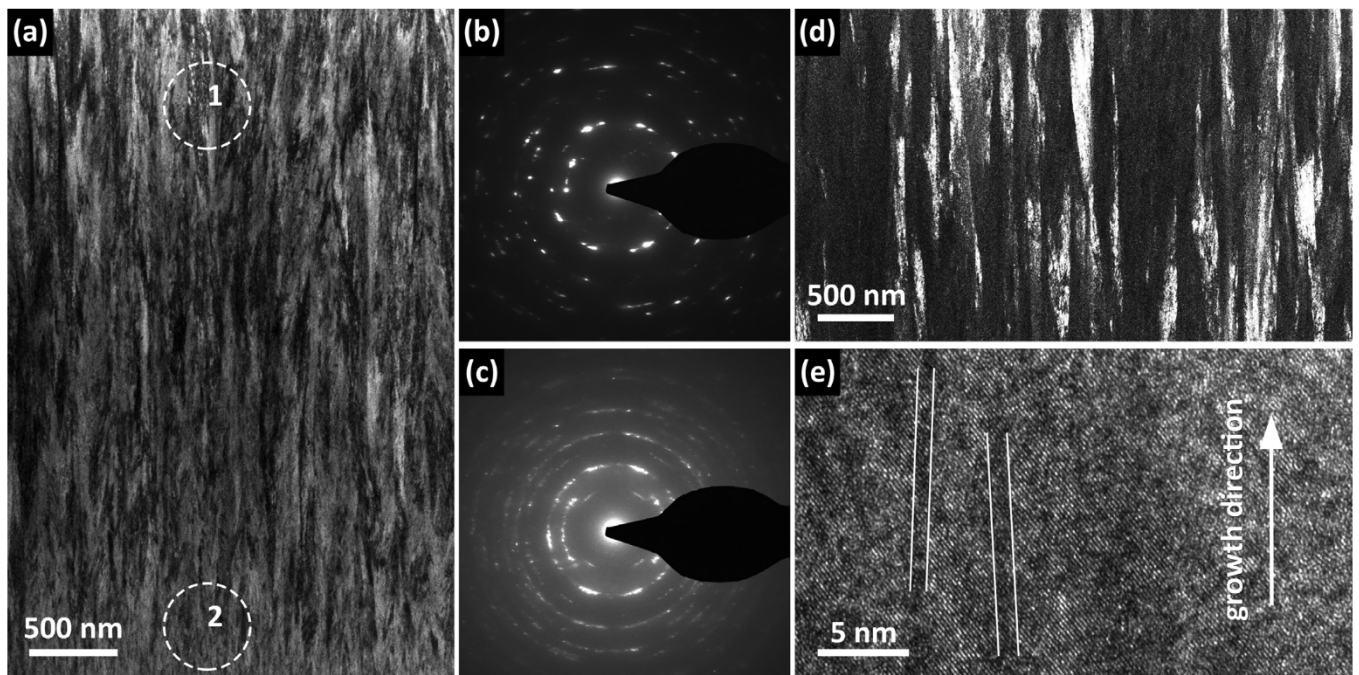


Fig. 5. Cross-sectional TEM investigations of $(\text{Hf,Ta,V,W,Zr})\text{B}_2$ deposited with $U_{\text{bias}} = -60 \text{ V}$. (a) Bright field TEM image; (b) SAED pattern of area 1 indicated by the dashed circle in (a); (c) SAED pattern of area 2 indicated by the dashed circle in (a); (d) dark field TEM image; (e) high-resolution TEM image where lower density regions are indicated with white lines.

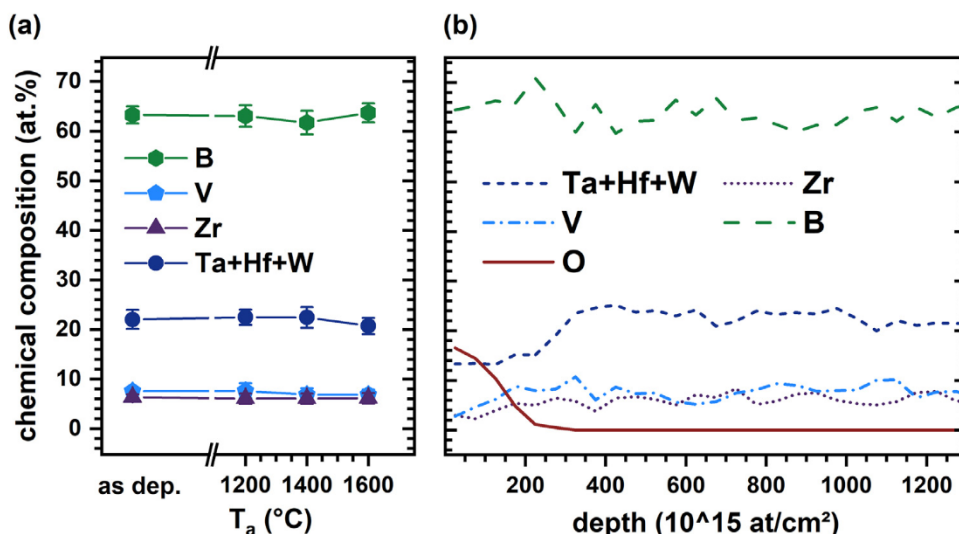


Fig. 6. (a) ERDA obtained chemical composition of $(\text{Hf,Ta,V,W,Zr})\text{B}_2$ coating deposited with $U_{\text{bias}} = -60$ V on sapphire substrates after vacuum-annealing at $T_a = 1200, 1400$, and 1600°C . (b) ERDA obtained depth profile of the sample annealed at 1200°C .

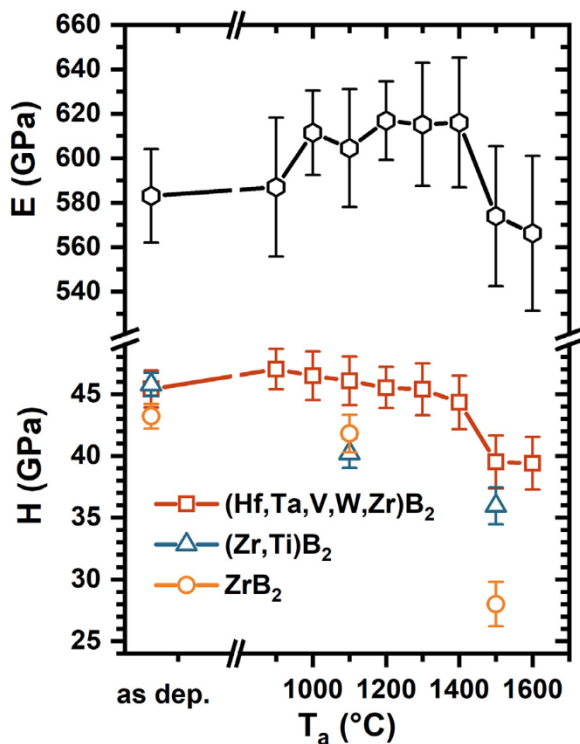


Fig. 7. Indentation modulus E and hardness H of $(\text{Hf,Ta,V,W,Zr})\text{B}_2$ deposited with $U_{\text{bias}} = -60$ V on sapphire substrates after vacuum-annealing at $T_a = 900, 1000, 1100, 1200, 1300, 1400, 1500$, and 1600°C for 10 min. For comparison we added the data of ZrB_2 and $(\text{Zr,Ti})\text{B}_2$ from Ref.[17].

DC sputter power density was 4.7 W/cm^2 , and the substrate bias potentials were either $-40, -60, -80$, or -100 V. If we assume an average melting temperature T_m of around 3240 K (from a linear interpolation of all the corresponding diborides), the 450°C ($\sim 723 \text{ K}$) yields a homologues temperature (T_s/T_m) of ~ 0.22 [21–25]. Fracture cross sections of our coatings are studied with a FEI Quanta 200 SEM – equipped with a field emission gun (FEG) and operated at an acceleration voltage of 10 kV – for their growth morphology. Their chemical composition was obtained by top-view investiga-

tions via energy dispersive X-ray spectroscopy (EDS) using a FEI Philips XL30 SEM equipped with an EDAX EDS detector. The boron content was additionally evaluated for the sample prepared with -60 V bias by time-of-flight elastic recoil detection analysis (TOF-ERDA) with a recoil detection angle of 45° using a 36 MeV I^{8+} ion beam. This coating was studied in its as-deposited state as well as after the 10-min-vacuum-annealing at $1200, 1400$, and 1600°C (next but one paragraph) by TOF-ERDA. Details of the method, employed set-up, and accelerator are described elsewhere [26],[27]. Transmission electron microscopy (TEM) images as well as selected area electron diffraction (SAED) patterns were obtained using a TECNAI F20 FEG-TEM operated at 200 keV .

Coatings on sapphire substrates as well as coating material removed from low alloy steel foil (by chemically dissolving the foil with a diluted HNO_3) are characterized by XRD using a PANalytical XPert Pro MPD (θ - θ diffractometer) equipped with a $\text{Cu-K}\alpha$ ($\lambda = 1.54 \text{ \AA}$) radiation source. Mechanical properties, indentation modulus E and hardness H , of the coatings on sapphire substrates (in their as-deposited state and after vacuum annealing, next paragraph) were obtained by evaluating nanoindentation load-displacement curves according to the method from Oliver and Pharr [28]. For this we used a UMIS II nanoindentation system and recorded 45 load-displacement curves for each measurement point, starting at a load of 32 mN and decreasing the load in 0.5 mN steps down to 10 mN . The maximum indentation depth was always below 210 nm and hence significantly below 10% of the coating thickness, which was $\sim 6.5 \text{ }\mu\text{m}$.

Powder samples as well as coatings on sapphire substrates (prepared with -60 V bias potential) were vacuum annealed in a Centorr LF22-2000 vacuum furnace (base pressure 0.8 mPa) at T_a (varied between 900 and 1600°C in 100°C steps) for 10 min. The heating rate was 20 K/min and the cooling rate (passively, by turning-off the heater) down to 200°C was $> 50 \text{ K/min}$. After these heat treatments the samples were again investigated by XRD, nanoindentation, and EDS.

Furthermore, the coatings prepared with -60 V bias potential are studied in detail for the element distribution in their as-deposited state and after vacuum annealing at $1200, 1400$, and 1600°C with APT. The three-dimensional spatially-resolved chemical composition at the nanometer scale of $(\text{Hf,Ta,V,W,Zr})\text{B}_2$ was investigated using a CAMECA local electrode atom probe 4000X HR. Laser-assisted field evaporation was employed with 50 pJ laser

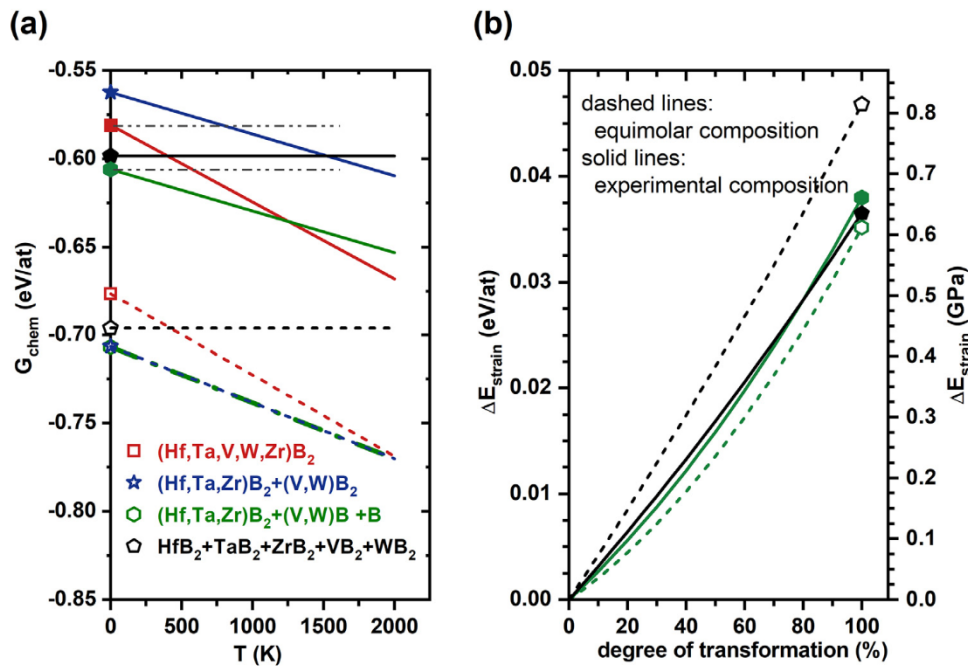


Fig. 8. (a) G vs. T curves for the high-entropy metal-sublattice diboride $(\text{Hf,Ta,V,W,Zr})\text{B}_2$, the sum of the diborides $(\text{Hf,Ta,Zr})\text{B}_2$ plus $(\text{V,W})\text{B}_2$, and the sum of $(\text{Hf,Ta,Zr})\text{B}_2$ plus $(\text{V,W})\text{B}$ plus B exhibiting lower energy of formation than the HESB. (b) Strain energy for decomposition of the HESB into the constituting binaries (black lines with pentagons) or into $(\text{Hf,Ta,Zr})\text{B}_2$ plus $(\text{V,W})\text{B}$ plus B (green lines with hexagons) depending on the degree of transformation. The dashed lines are for an equimolar composition and the solid lines are for a chemical composition close to the experimentally obtained values (by ERDA and EDS).

pulse energy, 200 kHz laser pulse frequency, and 60 K base temperature. The average detection rate was set to 1% and at least 15 million ions were obtained for each measurement. Needle-shape specimens were prepared by focused ion beam (FIB) techniques using a FEI Helios Nanolab 660 dual-beam microscope and following a standard approach [29]. These specimens were extracted parallel to the growth direction from powdered free-standing coating material. The region of interest was protected with a 350-nm-thin Pt layer against Ga implantation and this protection layer was removed during the final milling of the specimens.

The energy of formation of $(\text{Hf,Ta,V,W,Zr})\text{B}_2$, $(\text{Hf,Ta,Zr})\text{B}_2$ and $(\text{V,W})\text{B}_2$ in their AlB_2 prototype structure (space group 191 (P6/mmm), shortly α -type structure) is obtained by density functional theory (DFT) calculations employing the Vienna Ab Initio Simulation Package (VASP) [30]. Structure optimization was obtained by applying the projector augmented wave method within the general gradient approximation (GGA) parameterized by Perdew, Burke, and Ernzerhof [31], of solid solutions treated with the special quasirandom structure approach (applying the ATAT simulation package [32]). Energy cutoff and k-point mesh were chosen carefully, to ensure energy convergence of a few meV/at, for all calculations. To reach an equimolar composition of the $(\text{Hf,Ta,V,W,Zr})\text{B}_2$, for all diboride compositions a $5 \times 5 \times 2$ supercell was created (containing 150 atoms). For the calculations regarding $(\text{V,W})\text{B}$ (space group 63 (cmcm)), a $2 \times 2 \times 2$ supercell containing 64 atoms was chosen. The experimental composition for all calculations was taken from the EDS measurements. Furthermore, the elastic constants were calculated by applying the stress-strain-method [33]. These were used to determine the polycrystalline Young's modulus Y and the Poisson ratio [34–36].

To evaluate the strain energy density resulting from a phase transition of the solid solution $(\text{Hf,Ta,V,W,Zr})\text{B}_2$ phase into different daughter phases we apply continuum mechanics mean field theories. A phase transition generally leads to a change of specific volume, inducing eigenstrains which have to be accommodated by elastic deformation of the matrix and the newly formed phases.

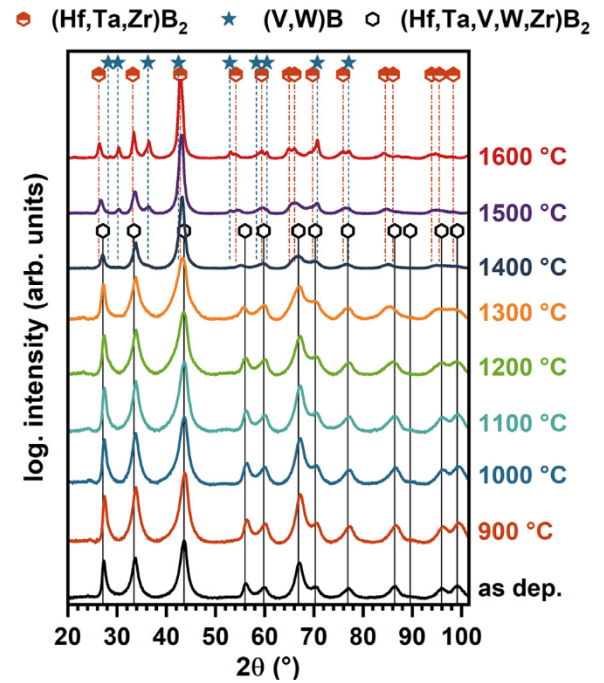


Fig. 9. XRD patterns of vacuum-annealed (at different temperatures, indicated next to the individual patterns) powdered free-standing coating material. The empty black hexagons indicate the XRD peak positions for an AlB_2 -structure with lattice parameters of $a = 3.09$ Å and $c = 3.28$ Å. The half-filled red hexagons indicate the XRD peak positions for an AlB_2 -structure with lattice parameters of $a = 3.11$ Å and $c = 3.39$ Å. Based on APT investigations (presented later) this is indicated with $(\text{Ta,Zr,Hf})\text{B}_2$. The blue stars mark the XRD peak positions for an orthorhombic structure (CrB-structure space group 63 (cmcm)) with lattice parameters of $a = 3.16$ Å, $b = 8.41$ Å, and $c = 3.06$ Å, which is indicated with $(\text{V,W})\text{B}$, also based on the APT investigations (presented later).

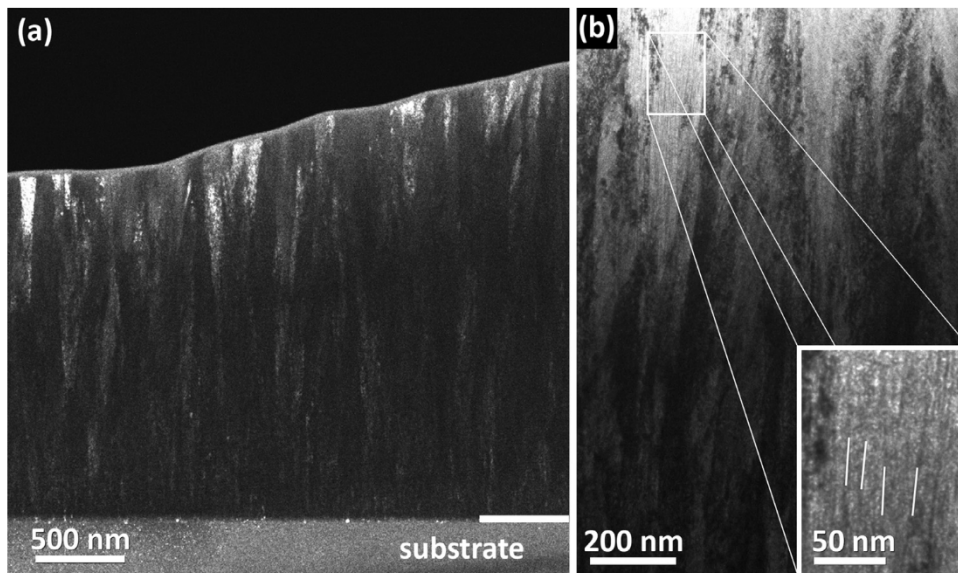


Fig. 10. Cross-sectional TEM investigations of (Hf,Ta,V,W,Zr) B_2 on sapphire substrates after vacuum annealing at 1400°C. (a) Dark field TEM image and (b) bright field TEM image with a higher resolution inset illustrating the more distinct (as compared to the as-deposited state) nanocolumnar structure elongated in growth direction.

The specific volumes of the phases V^P and the matrix V^M were taken from *ab initio* calculations. The volume change δ^P is then calculated by

$$\delta^P = \frac{V^P - V^M}{V^M}.$$

For all constituents, isotropic material behaviour is considered with polycrystalline elastic properties obtained by applying the Voigt-Reuss scheme to the *ab initio* calculated stiffness tensor. The precipitates are assumed to be of spherical shape with purely volumetric transformation strains, hence, the eigenstrain tensor is calculated by

$$\varepsilon_{ij}^{*P} = \frac{\delta^P}{3} \cdot \delta_{ij}$$

with δ_{ij} being the unity tensor. To account for the different eigenstrains and their interactions in a multiphase system, we used a Mori-Tanaka-based Transformation Field Analysis [37],[38]. Boundary conditions are set to correspond with vanishing macroscopic strains, whereas the macroscopic stresses are nonzero. We assume simultaneous formation of the daughter phases and study the strain energy density as a function of the degree of transformation.

3. Results and discussion

The EDS obtained chemical compositions of the different (Hf,Ta,V,W,Zr) diboride coatings suggest an almost MeB_2 stoichiometry with boron contents between 65 and 66 at%, independent of the bias potential used, Fig. 1a. The composition depth profile obtained by ERDA for the sample prepared with $U_{bias} = -60$ V reveals 63 ± 1.7 at% B, Fig. 1b, in excellent agreement with EDS data. The contents of the metallic elements are ~12 at% W, ~9 at% Hf, ~6 at% Ta, ~5 at% V, and ~4 at% Zr. Due to the energetically similar shell transitions of W and Zr, they are hard to separate by EDS, but ERDA indicates a Zr content of 6.6 at% and a V content of 7.8 at%. However, by ERDA the elements Hf, Ta, and W (neighbours in the periodic table) are difficult to separate. Nevertheless, except for a slight O-enriched surface, the depth-profile from the ERDA measurement indicates a homogenous element distribution over the whole sample volume investigated.

The individual samples show chemical composition variations within the error of EDS measurements (± 1 at%), therefore we conclude that their average chemistry is independent of the bias potential used during this investigation. Based on EDS, and normalising to stoichiometric MeB_2 , the nomenclature of the coatings corresponds to $(Hf_{0.25}Ta_{0.17}V_{0.14}W_{0.33}Zr_{0.11})B_2$. This causes a configurational entropy ΔS_{conf} of $1.53 \cdot R$ per formula unit, and classifies the synthesised diborides as high-entropy metal-sublattice diborides (HESB) according to the above-mentioned definition ($\Delta S_{conf} \geq 1.5 \cdot R$). Using the Zr and V contents from ERDA (which are higher than those obtained from EDS) the configurational entropy is even higher, as the metal-sublattice is closer to an equimolar composition.

All coatings exhibit a fine-fibrous growth morphology (independent of the bias potential applied, Fig. 2a-d) with a nearly featureless appearance for the initial growth region close to the sapphire substrate. With increasing bias potential from -40 to -100 V the growth rate only slightly decreases from ~110 to ~80 nm/min.

XRD investigations of all coatings clearly demonstrate a single-phase solid solution diboride with α -structure, see Fig. 3 exemplarily showing XRD patterns of coatings grown on sapphire. For $U_{bias} = -40$ V these show a preferred (112)-oriented growth that changes towards a (111)-oriented growth with increasing U_{bias} to -100 V, Fig. 3.

The XRD peak positions of this HESB suggest lattice parameters of $a = 3.09$ Å and $c = 3.28$ Å. These are in very good agreement with the linearly interpolated lattice parameters between HfB_2 , TaB_2 , VB_2 , WB_2 , and ZrB_2 (from ICDD reference data) – using their above-mentioned chemical composition – which are $a = 3.08$ Å and $c = 3.24$ Å.

Indentation modulus E and hardness H of the samples are ~580 GPa and ~45 GPa, respectively, independent of the substrate bias potential applied, Fig. 4. The individual values are within the error of measurement of about ± 20 GPa for E and ± 1.5 GPa for H . This is also because the growth morphology is nearly independent of the bias potential used, and already for a relatively low U_{bias} of -40 V, a rather dense fine-fibrous growth morphology is obtained, Fig. 2. The relatively constant mechanical properties for the different bias potentials suggest that these are also independent of the preferred growth orientation, which does change with the bias potential (see Fig. 3).

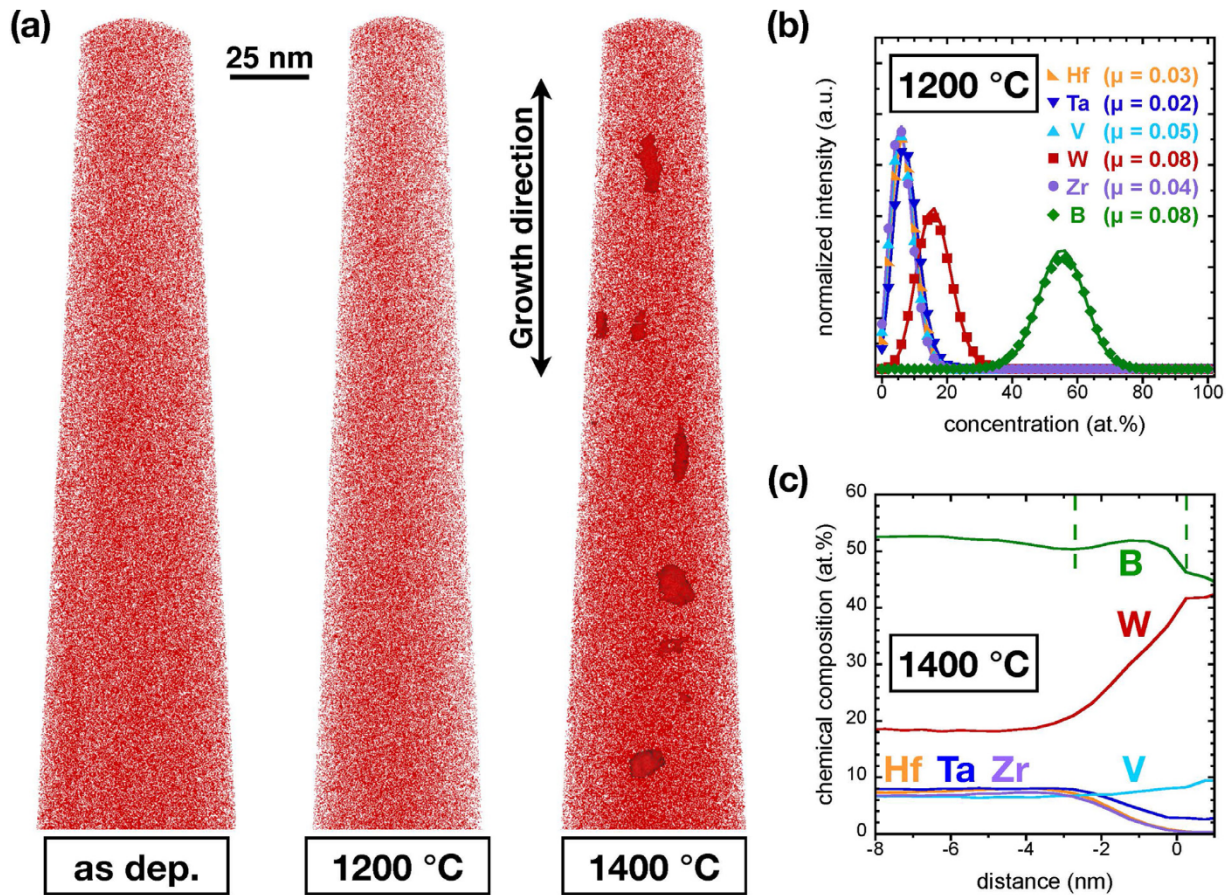


Fig. 11. Local chemical composition analysis of as-deposited as well as 1200 and 1400 °C annealed (Hf,Ta,V,W,Zr)B₂ at the nanometer scale. (a) Reconstruction of W atomic positions. W-rich regions are indicated by isoconcentration surfaces with ≥ 35 at% and evident after annealing at 1400 °C. (b) Frequency distribution analysis after annealing at 1200 °C. While data points represent the measured distribution of the elements, lines in the corresponding colour code indicate a random, binomial distribution. Pearson correlation coefficients are provided in brackets. (c) Proximity histogram of the W-rich regions with ≥ 35 at% after annealing at 1400 °C. The dashed lines emphasise a confined B enrichment at the interface region.

Detailed cross-sectional TEM studies of (Hf,Ta,V,W,Zr)B₂ prepared with $U_{\text{bias}} = -60$ V clearly confirm the dense fine-fibrous growth morphology, Fig. 5. At the interface to the substrate, their grain size is small, typical for random nucleation, followed by a competitive growth region. But even near to the coating surface, the column diameters are still rather small with about 80 – 100 nm, see Fig. 5a. The corresponding SAED investigations show distinct diffraction spots, Fig. 5b, highlighting the oriented columns with a large aspect ratio. The aperture size is indicated with a dashed circle in Fig. 5a, which is easily exceeded by a column length. Contrary, close to the substrate-coating interface the aperture size covers several column lengths and thus the corresponding SAED pattern is more ring-like rather than having distinct diffraction spots, Fig. 5c. The large aspect ratio of the columns close to the coating's surface is easily seen in the higher resolution dark field TEM image, Fig. 5d, suggesting for $\sim 1 \mu\text{m}$ long and 50 nm wide columns. The contrast modulations during high-resolution TEM investigations (indicated by white lines in Fig. 5e) point towards a periodic chemical and/or strain variation along the relatively dense columns.

After vacuum-annealing at $T_a = 1200, 1400$, and 1600°C , the investigated coating still shows the same average chemical composition as in their as-deposited state, see the ERDA results summarised in Fig. 6a. Even the boron content stays at ~ 62 at%, contrary to previous studies on high-entropy metal-sublattice diborides or Ti-B-N, where a significant B-loss upon vacuum-annealing was observed on the account of volatile H₃BO₃ forma-

tion [17,39]. Also, the ERDA depth profile of the coating annealed at 1200 °C suggests only for a small surface-near region enriched in oxygen. The very similar O-depth profile to the as-deposited state indicates that there is no significant oxygen uptake during vacuum annealing.

Nanoindentation measurements of these coatings ($U_{\text{bias}} = -60$ V, sapphire substrate) after vacuum-annealing also suggest excellent thermal stability, at least up to 1400 °C. Their indentation modulus slightly increases from 580 ± 20 GPa to 610 ± 30 GPa upon annealing at T_a up to 1400 °C, respectively, Fig. 7. If no phase transformation takes place, this indicates that the vacancy content decreases and/or the cohesive strength of grain or column boundary regions increases [39]. Both would be caused by the annealing treatment as thin films prepared by magnetron sputtering (at low homologues temperatures, as in the present case) typically exhibit an extensive vacancy content and underdense boundary regions [40]. Increasing T_a further to 1500 and 1600 °C leads to a noticeable reduction in E to ~ 570 GPa.

The hardness of the (Hf,Ta,V,W,Zr)B₂ coating initially increases upon vacuum annealing, from 45.4 ± 1.5 to 47.0 ± 1.6 GPa with $T_a = 900^\circ\text{C}$. Raising T_a to 1400 °C causes a small but continuous decrease to 44.3 ± 2.1 GPa. Similar to the behaviour of the indentation modulus, also the hardness shows a more distinct reduction upon further increasing T_a to 1500 and 1600 °C. After which the hardness was “only” about 39.5 GPa, see Fig. 7.

These results indicate that a relatively small grain size and a high defect density (point defects due to the high-entropy metal-

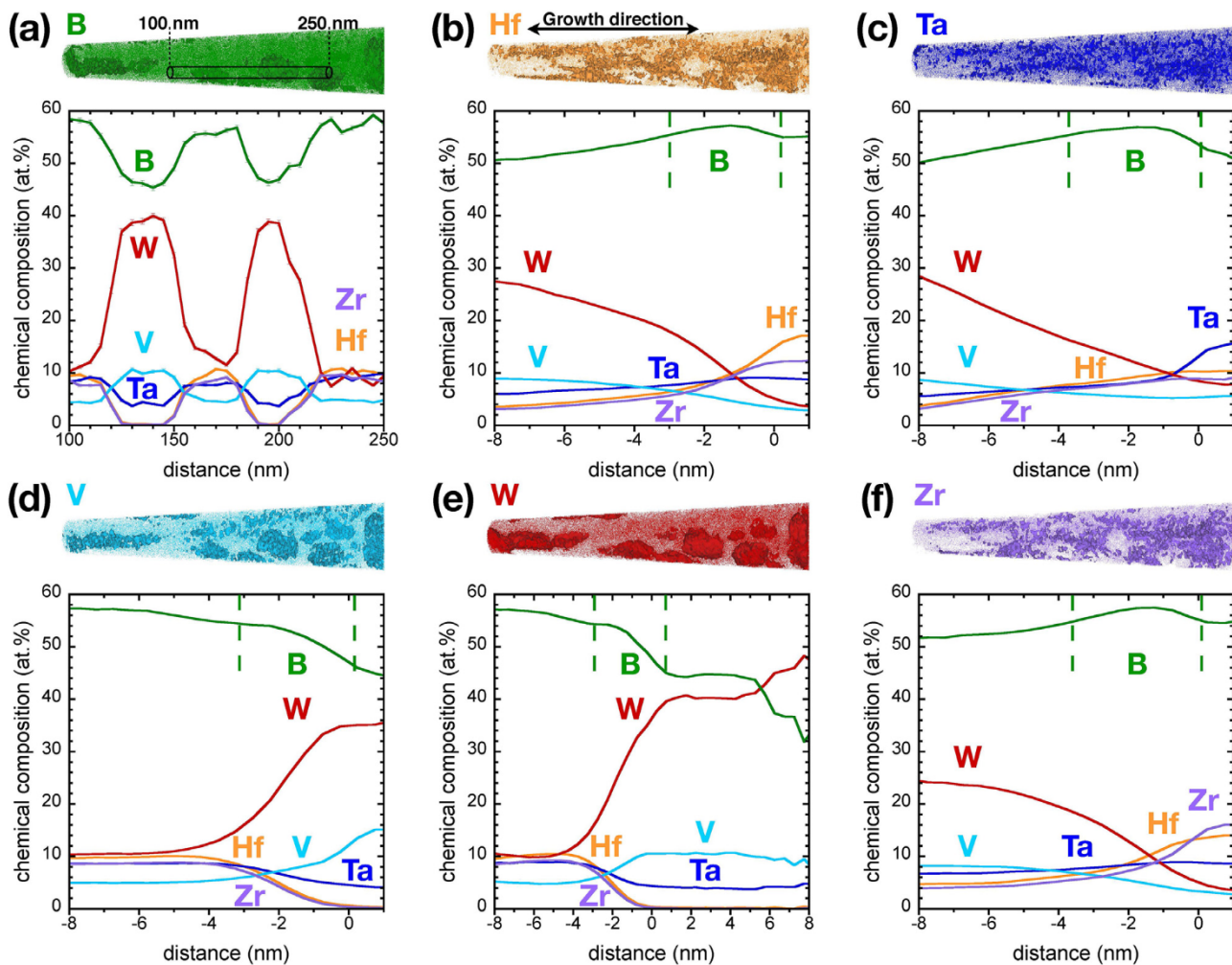


Fig. 12. Local chemical composition analysis of 1600°C annealed (Hf,Ta,V,W,Zr) B_2 at the nanometer scale. (a) Reconstruction of B atomic positions and B-rich regions are indicated by isoconcentration surfaces with ≤ 46 at%. The chemical composition profile originates from the region indicated by a cylinder within the reconstruction of B atomic positions. Proximity histograms are shown from (b) Hf-rich regions with ≥ 13 at%, (c) Ta-rich regions with ≥ 11 at%, (d) V-rich regions with ≥ 11 at%, (e) W-rich regions with ≥ 35 at% and (f) Zr-rich regions with ≥ 12 at%. The length of each reconstructed APT specimen is 300 nm. The dashed lines in (b)–(f) emphasise a confined B enrichment in the interface region.

sublattice, see next but one paragraph, and dislocations) is maintained leading to the preserved superhardness ($H \geq 40$ GPa) up to $T_a = 1400^\circ\text{C}$. Thermally-induced recovery effects may essentially influence the vacancy content (to reach thermal equilibrium) and underdense boundary regions upon which the indentation modulus and hardness even increase up to $T_a = 1400^\circ\text{C}$. The more distinct decrease in E and H upon annealing at $T_a = 1500$ and 1600°C is due to the decomposition of the high-entropy metal-sublattice diboride, (Hf,Ta,V,W,Zr) B_2 , towards a (Hf,Ta,Zr) B_2 diboride and (V,W)B monoboride (the corresponding XRD studies are presented later). The binary ZrB_2 or ternary (Zr,Ti) B_2 (prepared with the same deposition equipment) show a significantly lower thermal stability, with a more pronounced impact of the annealing temperature especially on the hardness [17], see Fig. 7.

For an equimolar composition, the solid solution HESB phase has a less negative energy of formation (E_f) – see Fig. 8a (y-axis value for 0 K, obtained by *ab initio* calculations) – than the corresponding binaries. This is also valid for the other equimolar cases considered here [(Hf,Ta,Zr) B_2 + (V,W) B_2 and (Hf,Ta,Zr) B_2 + (V,W)B + B]. Hence, the formation of a single-phase HESB is least preferred. Contrary, for metal contents close to the experimentally obtained chemical composition, the HESB is already

preferred at 0 K over the sum of (Hf,Ta,Zr) B_2 + (V,W) B_2 diboride formation, but again loses against the respective binaries and especially the formation of (Hf,Ta,Zr) B_2 + (V,W)B + B. Simply using the configurational entropy (with $S_{\text{conf}} = -R \sum_{i=1}^5 x_i \ln x_i$ and x_i being the molar fraction of the constituting binary diborides) and the energy of formation E_f of the solid solutions for the mixing enthalpy (H_{mix}) we obtained the Gibbs free energy ($G_{\text{chem}} = H_{\text{mix}} - TS_{\text{conf}}$).

Both scenarios (equimolar as well as that close to the experimentally obtained chemical composition) show that the high-entropy metal-sublattice diboride solid solution is clearly metastable compared to the individual binaries, see Fig. 8a. However, at temperatures above 500 K the configurational entropy contribution from the metal-sublattice is overcompensating the mixing enthalpy difference rendering the metastable solid solution (red lines with squares) stable over the individual binaries (black lines with pentagons). These calculations assume the enthalpy of formation to be independent of temperature and only consider configurational contributions to the entropy term.

Furthermore, the decomposition of (Hf,Ta,V,W,Zr) B_2 into (Hf,Ta,Zr) B_2 plus (V,W)B plus B, which is observed by APT, is considered in the calculations. This scenario shows an even lower

G_{chem} with $T < 2000$ K for the equimolar scenario, and with $T < 1250$ K for the experimentally determined composition. The fact that our prediction renders $(\text{Hf,Ta,V,W,Zr})\text{B}_2$ as more stable than the experimentally verified multi-phase decomposition scenario – at the experimentally determined decomposition temperature – may be rationalised by considering the above described limitations of the here employed basic computational strategy. For example, we have not treated the temperature dependence of the enthalpies as well as the thermal entropy contributions.

The significantly more negative energy of formation for the multi-phase decomposition scenario $[(\text{Hf,Ta,Zr})\text{B}_2 \text{ plus } (\text{V,W})\text{B plus B}]$; green lines with hexagons in Fig. 8) would suggest that the formation out of $(\text{Hf,Ta,V,W,Zr})\text{B}_2$ (red lines with cubes in Fig. 8) occurs at quite “low” temperatures (as soon as diffusion is possible); the energy gap (driving force for decomposition) between $(\text{Hf,Ta,V,W,Zr})\text{B}_2$ and these decomposition products is rather large. But please consider that in solid-solid phase transitions an additional amount of energy, the strain energy, caused by the differences in specific volumes of the phases, has to be overcome. Consequently, the products become steadily more unfavourable with increasing degree of transformation, see Fig. 8b. The decomposition of $(\text{Hf,Ta,V,W,Zr})\text{B}_2$ towards $(\text{Hf,Ta,Zr})\text{B}_2$ plus $(\text{V,W})\text{B}$ plus B causes an increasing strain energy with increasing degree of transformation, retarding or even limiting the process. The equimolar composition would lead to slightly lower retarding energies than the near-to-experimental composition (see dashed and solid green lines with hexagons in Fig. 8b, being 0.035 eV/at (0.57 kJ/cm³ or GPa) and 0.038 eV/at (0.65 kJ/cm³ or GPa), respectively, for a complete transformation. For comparison we also calculated the associated strain energy for a decomposition towards the binary phases, yielding a similar strain energy for the near-to-experimental composition, but higher one for the equimolar composition (black lines with pentagons in Fig. 8b). The balance between driving and retarding energies for the decomposition of the HESB (Fig. 8a and b) is also the reason, why we observe the decomposition not immediately at temperatures where diffusion would be sufficient (in addition to the energy required for the formation of new interfaces [41] and distribution of elements, summarised in nucleation processes).

Detailed XRD studies of powdered free-standing coating material after the individual vacuum-annealing treatments allow drawing a picture of their thermal stability and decomposition processes, Fig. 9. In the as-deposited state, the pattern clearly shows a single-phase solid solution with AlB_2 -prototype structure having lattice parameters of $a = 3.09$ Å and $c = 3.28$ Å. Identical values were obtained for the coating grown on sapphire substrates (Fig. 3), but here no preferred growth orientation can be detected as we analysed powdered coating material. The latter is essential to avoid detrimental substrate interference and interactions during annealing at these rather high temperatures up to 1600°C. The coatings remain single phased up to $T_a = 1300^\circ\text{C}$ and also the XRD peak positions and shapes are relatively unaffected, suggesting for constant lattice parameters, macro- and microstresses. The full width at half maximum even slightly increases when increasing T_a to 1300°C, suggesting actually an increased lattice distortion. Only when increasing T_a further to 1400°C the formation of additional small XRD peaks at diffraction angles of ~ 30 and ~ 33 deg can be detected, and the widths of the XRD peaks from the remaining matrix decreases. After annealing at even higher temperatures, these small XRD peaks (from the emerging phase) further increase in intensity and additional ones can be detected (see the pattern for $T_a = 1600^\circ\text{C}$), from which it was possible to identify the crystal structure. The additional XRD peaks (indicated by blue stars in Fig. 9) suggest the formation of an orthorhombic structure with lattice parameters of $a = 3.16$ Å, $b = 8.41$ Å, and $c = 3.06$ Å. Detailed APT investigations indicate a separation of the high-entropy

metal-sublattice $(\text{Hf,Ta,V,W,Zr})\text{B}_2$ towards $(\text{Hf,Ta,Zr})\text{B}_2$ and $(\text{V,W})\text{B}$ upon annealing at $T_a \geq 1400^\circ\text{C}$. Therefore, we used the WB reference pattern (ICDD 00-006-0541) and adopted the lattice parameter for a solid solution $(\text{V,W})\text{B}$, which is in excellent agreement with the additional XRD peaks. Simultaneously with the formation of this new phase, the XRD peak positions of the solid-solution AlB_2 -structure shift to lower diffraction angles. Based on detailed APT investigations (presented later) we named the remaining matrix $(\text{Hf,Ta,Zr})\text{B}_2$. The XRD peak positions of this solid solution suggest for lattice parameters of $a = 3.11$ Å and $c = 3.39$ Å (indicated by half-filled red hexagons in Fig. 9). The interpolated lattice parameters, according to ICDD reference patterns for HfB_2 , TaB_2 , and ZrB_2 (using mole fractions relevant for our chemical composition) are with $a = 3.13$ Å and $c = 3.41$ Å in excellent agreement.

Even after annealing at 1400°C – where already first indications for a phase separation of the solid-solution $(\text{Hf,Ta,V,W,Zr})\text{B}_2$ could be detected by XRD – the coating (for this study we used a coated sapphire substrate) still shows the dense fine-fibrous growth morphology, very similar to the as-deposited state (compare Figs. 10a and 5a). However, TEM investigations suggest that the microstructural feature (being elongated in growth direction and presumably caused by boron segregation, already present in the as-deposited state) is more distinct after annealing at 1400°C, see Fig. 10b and especially the higher magnification inset.

Spatially-resolved chemical composition analysis at the nanometer scale of powdered free-standing coating material reveals a random distribution of all elements in the as-deposited state, represented by the reconstruction of W atomic positions in Fig. 11a. Also, after annealing at 1200°C the distribution of elements is still random based on the frequency distribution analysis shown in Fig. 11b. The measured distribution of the constitutional elements (data points) is compared to a random, binomial distribution (lines in corresponding colour code). The Pearson correlation coefficients μ are < 0.1 for all elements which indicates a random elemental distribution. After annealing at $T_a = 1400^\circ\text{C}$ the formation of W-rich regions is evident from the APT data. W-rich regions with ≥ 35 at% are indicated by isoconcentration surfaces. These data suggest an elongated formation along the growth direction, where especially column boundaries are preferred sites to easier accommodate evolving strains (see Fig. 8b) and provide higher diffusivities (even spinodal decomposition preferably starts at column boundaries [42]). The proximity histogram of these regions after annealing at 1400°C, Fig. 11c, reveals that V as well as Ta are present in the W-rich regions, while Hf and Zr are depleted. Further characteristic is that with increasing W content also the B content decreases, which indicates that the stoichiometry changes from MeB_2 towards MeB in the W-rich region. Furthermore, a confined B enrichment is visible at approximately 0 to -2 nm (indicated by dashed lines) and hence at the interface between the W-rich region and the matrix.

After annealing at an even higher temperature ($T_a = 1600^\circ\text{C}$) decomposition of the $(\text{Hf,Ta,V,W,Zr})\text{B}_2$ solid solution is observed by APT in agreement with XRD data. The chemical composition profile in Fig. 12a reveals the formation of V- and W-rich regions with up to 10 at% V and 40 at% W, while Hf and Zr are depleted and Ta is present with approximately 4 at%. Also evident is that the B concentration decreases from approximately 58 to 46 at% in the V- and W-rich regions. The APT-quantified absolute B concentrations are significantly smaller than the average concentrations obtained by ERDA and preferential B retention has been reported for DC magnetron sputtered ZrB_2 thin films [43]. Nevertheless, the observed decrease of the B concentration from the matrix towards the V- and W-rich region in combination with XRD data (Fig. 9) indicates the formation of $(\text{V,W})\text{B}$ with soluted Ta.

Proximity histograms of Hf, Ta, V, W, and Zr (Fig. 12b-f) after annealing at 1600°C reveal the local enrichment of each

metal and it is evident that also the chemical composition of the (Hf,Ta,V,W,Zr) B_2 matrix is significantly altered. Interestingly, all of the interface regions are characterized by a confined B enrichment after annealing at 1600°C and the corresponding regions are emphasised by dashed lines. Such confined B enrichment has been also observed for the W-rich regions after annealing at 1400°C, compare Fig. 11c. Based on the combination of ERDA (indicating no B-loss due to annealing at 1400 or 1600°C, Fig. 6), TEM, and APT data, we can conclude that the decomposition from (Hf,Ta,V,W,Zr) B_2 towards (Hf,Ta,Zr) B_2 plus (V,W)B is accompanied by the formation of a B-rich interface region between these phases. Why V and W are concentrated in the monoboride and Hf, Ta, and Zr basically remain in the diboride can be understood based on the melting points T_m of the individual binary borides. HfB $_2$, TaB $_2$, and ZrB $_2$ have T_m values between 3400 and 3600 K, but VB $_2$ and WB $_2$ (actually W $_2$ B $_5$) only exhibit a T_m of ~3000 and 2638 K, respectively. The monoboride of W exhibits with ~2940 K actually an even higher melting point than its diboride [21–25].

4. Summary and conclusions

Single-phase AlB $_2$ -structured diborides with a high-entropy metal-sublattice (HESB), (Hf,Ta,V,W,Zr) B_2 , were deposited by non-reactive magnetron sputtering of a powder-metallurgically prepared diboride target composed of 20 mol% HfB $_2$, TaB $_2$, VB $_2$, W $_2$ B $_5$, and ZrB $_2$. Chemical composition, growth morphology (dense fine-fibrous), crystal structure (AlB $_2$ -type) as well as mechanical properties ($E \sim 580$ GPa and $H \sim 45$ GPa) are essentially independent on the bias potential ($U_{bias} = -40, -60, -80, -100$ V) used during their preparation (at a substrate temperature of 450°C). The EDS and ERDA obtained B content is with ~62 at% close to MeB $_2$ stoichiometry. The configurational entropy of the metal-sublattice yields 1.53-R for the prepared (Hf $_{0.25}$ Ta $_{0.17}$ V $_{0.14}$ W $_{0.33}$ Zr $_{0.11}$)B $_2$, classifying it as high-entropy (> 1.5 -R) sublattice diboride. *Ab initio* based calculations indicate that the high-entropy metal-sublattice ensures that the synthesised HESB is energetically more stable at $T > 1250$ K than the decomposition products (Hf,Ta,Zr) B_2 plus (V,W)B plus B.

Based on XRD studies the coatings remain single-phased AlB $_2$ -structured – with essentially the same lattice parameters and microstresses as in the as-deposited state – even when vacuum-annealed at temperatures up to 1300°C. APT indicates that also the distribution of the elements is random in the as-deposited state as well as after vacuum annealing at $T_a = 1200^\circ\text{C}$. Only after annealing at higher temperatures ($T_a \geq 1400^\circ\text{C}$) the formation of an additional phase can be detected by XRD, which was indicated by APT to be a (V,W)B monoboride with soluted Ta. The remaining matrix appears to be an AlB $_2$ -structured (Hf,Ta,Zr) B_2 (with soluted V and W). Additionally, as the overall boron content is constant over the annealing temperature, the formation of confined B-enriched regions during decomposition takes place. Due to this decomposition the indentation modulus and hardness of (Hf,Ta,V,W,Zr) B_2 decreased to ~570 GPa and ~40 GPa, respectively, when annealed at 1500 and 1600°C. The probably rather small volume fraction of the newly-formed W-rich regions with $T_a = 1400^\circ\text{C}$ has almost no influence on the mechanical properties, which are still very high with $E \sim 610$ GPa and $H \sim 44$ GPa.

Based on our results we can conclude that (Hf,Ta,V,W,Zr) B_2 coatings are superior to constituting diborides on account of their thermal stability and maintained mechanical properties. The random distribution of many different-sized metal species (resulting in a high-entropy metal-sublattice) guarantees for a maintained severe lattice distortion and consequently high microstresses even when annealed at 1300°C, allowing for the exceptional high hardness.

Declaration of Competing Interest

The authors declare that they have no known competing financial interests or personal relationships that could have appeared to influence the work reported in this paper.

The authors declare the following

Acknowledgments

This work was partly funded by the Austrian COMET Program (project K2 XTribology, no. 849109 and project K2 InTribology, no. 872176). The authors acknowledge the use of the X-ray center (XRC) and USTEM at TU Wien. They are also very grateful to Tomasz Wojcik (TU Wien, Austria) for assistance with TEM investigations and valuable discussions. Helmut Böhm (TU Wien, Austria) is acknowledged for assistance with the calculations of the strain energy. Support by the Swedish research council (Contract No. 821-2012-5144) and the Swedish Foundation for Strategic Research (Contract No. RIF14-0053) supporting accelerator operation is gratefully acknowledged. Plansee Composite Materials GmbH is acknowledged for support with target materials. J.M.S. acknowledges funding from the German research foundation (DFG) within the priority program SPP 2006 CCA-HEA.

References

- [1] B. Cantor, I.T.H. Chang, P. Knight, A.J.B. Vincent, Microstructural development in equiatomic multicomponent alloys, *Mater. Sci. Eng. A* 375–377 (2004) 213–218, doi:10.1016/j.msea.2003.10.257.
- [2] J.-W. Yeh, S.-K. Chen, S.-J. Lin, J.-Y. Gan, T.-S. Chin, T.-T. Shun, C.-H. Tsau, S.-Y. Chang, Nanostructured High-Entropy Alloys With Multiple Principal Elements: Novel Alloy Design Concepts And Outcomes, *Adv. Eng. Mater* 6 (2004) 299–303, doi:10.1002/adem.200300567.
- [3] B.S. Murty, J.W. Yeh, S. Ranganathan, High Entropy Alloys, Elsevier, 2014, doi:10.1016/B978-0-12-800251-3.00002-X.
- [4] A. Kirnbauer, A. Kretschmer, C.M. Koller, T. Wojcik, V. Paneta, M. Hans, J.M. Schneider, P. Polcik, P.H. Mayrhofer, Mechanical properties and thermal stability of reactively sputtered multi-principal-metal Hf-Ta-Ti-V-Zr nitrides, *Surf. Coat. Technol.* 389 (2020) 125674, doi:10.1016/j.surfcoat.2020.125674.
- [5] J. Gild, Y. Zhang, T. Harrington, S. Jiang, T. Hu, M.C. Quinn, W.M. Mellor, N. Zhou, K. Vecchio, J. Luo, High-Entropy Metal Diborides, A new class of high-entropy materials and a new type of ultrahigh temperature ceramics, *Sci. Rep.* 6 (2016) 2–11, doi:10.1038/srep37946.
- [6] Y. Zhang, W.M. Guo, Z. Bin Jiang, Q.Q. Zhu, S.K. Sun, Y. You, K. Plucknett, H.T. Lin, Dense high-entropy boride ceramics with ultra-high hardness, *Scr. Mater.* 164 (2019) 135–139, doi:10.1016/j.scriptamat.2019.01.021.
- [7] G. Anand, A.P. Wynn, C.M. Handley, C.L. Freeman, Phase stability and distortion in high-entropy oxides, *Acta Mater.* 146 (2018) 119–125, doi:10.1016/j.actamat.2017.12.037.
- [8] A. Sarkar, Q. Wang, A. Schiele, M.R. Chellali, S.S. Bhattacharya, D. Wang, T. Brezesinski, H. Hahn, L. Velasco, B. Breitung, High-entropy oxides: fundamental aspects and electrochemical properties, *Adv. Mater.* (2019) 1806236, doi:10.1002/adma.201806236.
- [9] A. Sarkar, R. Djenadic, D. Wang, C. Hein, R. Kautenburger, O. Clemens, H. Hahn, Rare earth and transition metal based entropy stabilised perovskite type oxides, *J. Eur. Ceram. Soc.* 38 (2018) 2318–2327, doi:10.1016/j.jeurceramsoc.2017.12.058.
- [10] T.J. Harrington, J. Gild, P. Sarker, C. Toher, C.M. Rost, O.F. Dippo, C. McElfresh, K. Kaufmann, E. Marin, L. Borowski, P.E. Hopkins, J. Luo, S. Curtarolo, D.W. Brenner, K.S. Vecchio, Phase stability and mechanical properties of novel high entropy transition metal carbides, *Acta Mater.* 166 (2019) 271–280, doi:10.1016/j.actamat.2018.12.054.
- [11] P. Sarker, T. Harrington, C. Toher, C. Osés, M. Samiee, J.P. Maria, D.W. Brenner, K.S. Vecchio, S. Curtarolo, High-entropy high-hardness metal carbides discovered by entropy descriptors, *Nat. Commun.* 9 (2018) 1–10, doi:10.1038/s41467-018-07160-7.
- [12] C.-H. Lai, M.-H. Tsai, S.-J. Lin, J. Yeh, Influence of substrate temperature on structure and mechanical properties of multi-element (AlCrTaTiZr) N coatings 201 (2007) 6993–6998, doi:10.1016/j.surfcoat.2007.01.001.
- [13] C.-H. Lai, S.-J. Lin, J.-W. Yeh, A. Davison, Effect of substrate bias on the structure and properties of multi-element (AlCrTaTiZr)N coatings, *J. Phys. D: Appl. Phys.* 39 (2006) 4628–4633, doi:10.1088/0022-3727/39/21/019.
- [14] C.H. Lai, S.J. Lin, J.W. Yeh, S.Y. Chang, Preparation and characterization of Al-Cr-Ta-Ti-Zr multi-element nitride coatings, *Surf. Coat. Technol.* 201 (2006) 3275–3280, doi:10.1016/j.surfcoat.2006.06.048.
- [15] S.Y. Chang, M.K. Chen, D.S. Chen, Multiprincipal-element AlCrTaTiZr-nitride nanocomposite film of extremely high thermal stability as diffusion barrier for Cu metallization, *J. Electrochem. Soc.* (2009) 156, doi:10.1149/1.3097186.

- [16] A. Kirnbauer, C. Spadt, C.M. Koller, S. Kolozsvári, P.H. Mayrhofer, High-entropy oxide thin films based on Al–Cr–Nb–Ta–Ti, *Vacuum* 168 (2019) 108850, doi:[10.1016/j.vacuum.2019.108850](https://doi.org/10.1016/j.vacuum.2019.108850).
- [17] P.H. Mayrhofer, A. Kirnbauer, P. Ertelthaler, C.M. Koller, High-entropy ceramic thin films; A case study on transition metal diborides, *Scr. Mater.* 149 (2018) 93–97, doi:[10.1016/j.scriptamat.2018.02.008](https://doi.org/10.1016/j.scriptamat.2018.02.008).
- [18] V. Moraes, C. Fuger, V. Paneta, D. Primetzhofer, P. Polcik, H. Bolvardi, M. Arndt, H. Riedl, P.H. Mayrhofer, Substoichiometry and tantalum dependent thermal stability of α -structured W-Ta-B thin films, *Scr. Mater.* 155 (2018) 5–10, doi:[10.1016/j.scriptamat.2018.06.005](https://doi.org/10.1016/j.scriptamat.2018.06.005).
- [19] V. Moraes, L. Zauner, T. Wojcik, M. Arndt, P. Polcik, H. Riedl, P.H. Mayrhofer, Thermally stable superhard diborides: an ab initio guided case study for V–W-diboride thin films, *Acta Mater.* 186 (2020) 487–493, doi:[10.1016/j.actamat.2020.01.014](https://doi.org/10.1016/j.actamat.2020.01.014).
- [20] C. Fuger, V. Moraes, R. Hahn, H. Bolvardi, P. Polcik, H. Riedl, P.H. Mayrhofer, Influence of Tantalum on phase stability and mechanical properties of WB₂, *MRS Commun.* 9 (2019) 375–380, doi:[10.1557/mrc.2019.5](https://doi.org/10.1557/mrc.2019.5).
- [21] P. Villars, H. Okamoto, eds., B–Hf Binary Phase Diagram 0–100 at% Hf: Datasheet from “PAULING FILE Multinaries Edition – 2012” in SpringerMaterials (https://materials.springer.com/isp/phase-diagram/docs/c_0905924).
- [22] P. Villars, H. Okamoto, eds., B–Ta Binary Phase Diagram 0–100 at% Ta: Datasheet from “PAULING FILE Multinaries Edition – 2012” in SpringerMaterials (https://materials.springer.com/isp/phase-diagram/docs/c_0902231).
- [23] P. Villars, H. Okamoto, eds., B–V Binary Phase Diagram 0–100 at% V: Datasheet from “PAULING FILE Multinaries Edition – 2012” in SpringerMaterials (https://materials.springer.com/isp/phase-diagram/docs/c_0903210).
- [24] P. Villars, H. Okamoto, eds., B–W Binary Phase Diagram 0–100 at% W: Datasheet from “PAULING FILE Multinaries Edition – 2012” in SpringerMaterials (https://materials.springer.com/isp/phase-diagram/docs/c_0103126).
- [25] P. Villars, H. Okamoto, eds., B–Zr Binary Phase Diagram 0–100 at% Zr: Datasheet from “PAULING FILE Multinaries Edition – 2012” in SpringerMaterials (https://materials.springer.com/isp/phase-diagram/docs/c_0907059).
- [26] P. Ström, P. Petersson, M. Rubel, G. Possnert, A combined segmented anode gas ionization chamber and time-of-flight detector for heavy ion elastic recoil detection analysis, *Rev. Sci. Instrum.* (2016) 87, doi:[10.1063/1.4963709](https://doi.org/10.1063/1.4963709).
- [27] M. Mayer, S. Möller, M. Rubel, A. Widdowson, S. Charisopoulos, T. Ahlgren, E. Alves, G. Apostolopoulos, N.P. Barradas, S. Donnelly, S. Fazinić, K. Heinola, O. Kakuee, H. Khodja, A. Kimura, A. Lagoyannis, M. Li, S. Markelj, M. Mudrinic, P. Petersson, I. Portnykh, D. Primetzhofer, P. Reichart, D. Ridikas, T. Silva, S.M. Gonzalez de Vicente, Y.Q. Wang, Ion beam analysis of fusion plasma-facing materials and components: facilities and research challenges, *Nucl. Fusion* 60 (2019) 25001, doi:[10.1088/1741-4326/ab5817](https://doi.org/10.1088/1741-4326/ab5817).
- [28] W.C. Oliver, G.M. Pharr, An improved technique for determining hardness and elastic modulus using load and displacement sensing indentation experiments, *J. Mater. Res.* 7 (1992) 1564–1583, doi:[10.1557/JMR.1992.1564](https://doi.org/10.1557/JMR.1992.1564).
- [29] K. Thompson, D. Lawrence, D.J. Larson, J.D. Olson, T.F. Kelly, B. Gorman, In situ site-specific specimen preparation for atom probe tomography, *Ultramicroscopy* 107 (2007) 131–139, doi:[10.1016/j.ultramic.2006.06.008](https://doi.org/10.1016/j.ultramic.2006.06.008).
- [30] G. Kresse, D. Joubert, From ultrasoft pseudopotentials to the projector augmented-wave method, *Phys. Rev. B – Condens. Matter Mater. Phys.* 59 (1999) 1758–1775, doi:[10.1103/PhysRevB.59.1758](https://doi.org/10.1103/PhysRevB.59.1758).
- [31] J.P. Perdew, K. Burke, M. Ernzerhof, Generalized gradient approximation made simple, *Phys. Rev. Lett.* 77 (1996) 3865–3868, doi:[10.1103/PhysRevLett.77.3865](https://doi.org/10.1103/PhysRevLett.77.3865).
- [32] A. Van de Walle, M. Asta, G. Ceder, The alloy theoretic automated toolkit: A user guide, *Calphad* 26 (2002) 539–553 *Comput. Coupling Phase Diagrams Thermochem.*, doi:[10.1016/S0364-5916\(02\)80006-2](https://doi.org/10.1016/S0364-5916(02)80006-2).
- [33] R. Yu, J. Zhu, H.Q. Ye, Calculations of single-crystal elastic constants made simple, *Comput. Phys. Commun.* 181 (2010) 671–675, doi:[10.1016/j.cpc.2009.11.017](https://doi.org/10.1016/j.cpc.2009.11.017).
- [34] Titrian, U. Aydin, M. Friák, D. Ma, D. Raabe, J. Neugebauer, Self-consistent scale-bridging approach to compute the elasticity of multi-phase polycrystalline materials, 2012. doi:[10.1557/opl.20141](https://doi.org/10.1557/opl.20141).
- [35] M. Friák, W.A. Counts, D. Ma, B. Sander, D. Holec, D. Raabe, J. Neugebauer, Theory-guided materials design of multi-phase Ti–Nb alloys with bone-matching elastic properties, *Materials (Basel)* 5 (2012) 1853–1872, doi:[10.3390/ma5101853](https://doi.org/10.3390/ma5101853).
- [36] L.F. Zhu, M. Friák, L. Lymperakis, H. Titrian, U. Aydin, A.M. Janus, H.O. Fabritius, A. Ziegler, S. Nikolov, P. Hemzalová, D. Raabe, J. Neugebauer, Ab initio study of single-crystalline and polycrystalline elastic properties of Mg-substituted calcite crystals, *J. Mech. Behav. Biomed. Mater.* 20 (2013) 296–304, doi:[10.1016/j.jmbbm.2013.01.030](https://doi.org/10.1016/j.jmbbm.2013.01.030).
- [37] G.J. Dvorak, Y. Benveniste, On transformation strains and uniform fields in multiphase elastic media, *Proc. R. Soc. Lond. Ser. A Math. Phys. Sci.* 437 (1992) 291–310, doi:[10.1098/rspa.1992.0062](https://doi.org/10.1098/rspa.1992.0062).
- [38] H.J. Böhm, *Stress and Strain Fields Due to Multiple Transforming Inhomogeneities*, ILSB Rep, 2005.
- [39] P.H. Mayrhofer, C. Mitterer, J.G. Wen, I. Petrov, J.E. Greene, Thermally induced self-hardening of nanocrystalline Ti–B–N thin films, *J. Appl. Phys.* (2006) 100, doi:[10.1063/1.2222406](https://doi.org/10.1063/1.2222406).
- [40] A. Anders, A structure zone diagram including plasma-based deposition and ion etching, *Thin Solid Films* 518 (2010) 4087–4090, doi:[10.1016/j.tsf.2009.10.145](https://doi.org/10.1016/j.tsf.2009.10.145).
- [41] P.H. Mayrhofer, L. Hultman, J.M. Schneider, P. Staron, H. Clemens, Spinodal decomposition of cubic Ti1–xAlxN: comparison between experiments and modeling, *Zeitschrift Fuer Met. Res. Adv. Technol.* 98 (2007) 1054–1059, doi:[10.3139/146.101570](https://doi.org/10.3139/146.101570).
- [42] R. Rachbauer, S. Massl, E. Stergar, D. Holec, D. Kiener, J. Keckes, J. Patscheider, M. Stiefel, H. Leitner, P.H. Mayrhofer, Decomposition pathways in age hardening of Ti–Al–N films, *J. Appl. Phys.* (2011) 110, doi:[10.1063/1.3610451](https://doi.org/10.1063/1.3610451).
- [43] D.L.J. Engberg, L. Tengdelius, H. Högborg, M. Thuvander, L. Hultman, Atom probe tomography field evaporation characteristics and compositional corrections of ZrB₂, *Mater. Charact.* 156 (2019) 109871, doi:[10.1016/j.matchar.2019.109871](https://doi.org/10.1016/j.matchar.2019.109871).
- [44] H. Holleck, *Binäre und ternäre Carbide- und Nitridsysteme der Übergangsmetalle*, in: G. Petzow (Ed.), *Materialkundlich-Technische Reihe 6*, Gebrüder Borntraeger, Berlin – Stuttgart, 1984, pp. 1–295.
- [45] H. Holleck, Material selection for hard coatings, *J. Vac. Sci. Technol. A* 4 (6) (1986) 2661–2669, doi:[10.1116/1.573700](https://doi.org/10.1116/1.573700).